Intramolecular modulation of iron-based metal organic framework with energy level adjusting for efficient photocatalytic activity

Haoyun Chen [a,b], Xingzhong Yuan [a,b,*], Longbo Jiang [a,b,*], Hou Wang [a,b], Hanbo Yu [a,b], Xinxin Wang [c]

[a] College of Environmental Science and Engineering, Hunan University, Changsha 410082, PR China
[b] Key Laboratory of Environmental Biology and Pollution Control (Hunan University), Ministry of Education, Changsha 410082, PR China
[c] College of Materials Science and Engineering, Hunan University, Changsha 410082, PR China

ARTICLE INFO

ABSTRACT

Efficient photocatalytic activity is always pressingly expected for photocatalytic technology on removing organic water contaminations. Modulating the intrinsic electronic properties is one of the most effective approaches to improve photocatalytic efficiency. Herein, we developed a promising photocatalyst through modulation electronic properties of iron-based metal organic framework by sulfur (S-MIL-53(Fe)), in which the sulfur particles were intramolecularly in-suite inserted into MIL-53(Fe) through annealing treatment process. The constructed S3-MIL-53(Fe) crystal with regular spindle-shaped polyhedron morphology exhibited superior higher apparent quantum efficiency (AQE) of 27.82% which was over 30 times than that of pure MIL-53(Fe) (0.903%) indicating the significantly enhanced photoactivity. A computational study was conducted to reveal the electronic structure changes and the resulted charge transfer induced by the sulfur modulation. The experimental and computational analyses suggest that intramolecular modulation MIL-53(Fe) with sulfur to engineer band structure for promoting charge transfer is a promising approach to improve the photocatalytic efficiency.

1. Introduction

Over recent decades, photocatalytic removal of organic pollutants has been an attractive approach to address traditional water treatment issues [1]. However, efficient photocatalytic activity is always limited by the original structure and electronic properties of the photocatalyst due to a multi-electron reaction process [2]. Therefore, substantial efforts have been dedicated to exploring more efficient and costive photocatalysts for organic pollutants removal [3]. Among which, newly porous crystalline materials of metal organic frameworks (MOFs) have attracted tremendous attentions for their high porosity, sufficient active sites, and transformable structures [4]. Over the past years, various nano-structured MOFs have been constructed by connecting metal-containing nodes with clusters and multifunctional organic ligands by coordination bonds [5]. Due to satisfactory electrochemical stability, MOFs have been comprehensively accepted as appealing candidates for photocatalytic applications [6–8]. Specifically, MIL-53(Fe) was fully certificated to be a semiconductor-like photocatalyst by the increased reports on photodegradation of the organic contamination

pollutants especially the tetracycline (TC) [9]. Their well photocatalytic activities can be attributed to the adequate small size and Fe (III)-oxide which acted as electronic transfer center to prevent the quick photo-generated electron-hole recombination [10]. As the most representative member of iron-based metal organic framework family, MIL-53(Fe) with plentiful Fe—O clusters received continuous investigations [11]. And their photocatalytic activities are reported to correlate with the covalent contribution, the coordination environment, structure of the active phases, the adsorption energies and oxidation states of the catalytically active metal centers [12].

However, due to the highly intricate complexity of fine-tuning the photocatalytic properties, superiorly enhancing the photocatalytic performance for MIL-Fe based photocatalyst is devoting extensive research efforts [13]. Tuning the structure and multifunctional the internal property for a targeted application have been a trend [14]. Among which modulating the internal electronic structures by introducing functional entities into MIL-Fe family is constantly reported to be an effective approach in constructing more preeminent photocatalyst [15]. For example, it was very recently reported that introducing cobalt into

---

MIL-Fe nanoparticles could significantly improve photocatalytic activity by adjusting band gap and optical absorption intensity [16]. Excellent catalytic performance was also realized through intramolecular modulating to construct iron-cobalt (oxy)phosphide nano-boxes by another work. These works certificated that the intramolecular electrons adjust intrinsic activity and can originally decide the catalytic performance. On the other hand, tracing from the origin promotional effect, the manner for intramolecular modulation is also of significant importance. It has been proved that modulation of the electronic structure with sulfur under thermodynamic conditions MOFs, can produce with higher intrinsic activity and optimal adsorption energies leading to exceptional photocatalytic performance and improved chemical stability [17–19]. As an example, the sulfur was used to modulate the structure of hexagonal boron nitride nanosheet (S-BNNS). The S-BNNS with adjusted lattice exhibited impressive visible light photocatalytic properties [20]. Thereby, improved photocatalytic properties are supposed to realize by the intramolecular modulated MIL-53(Fe) with sulfur atom. However, there are rare investigations on the specific design of customizable photocatalysts of S-MIL-53(Fe) with this approach. The effect of intramolecular sulfur on band structure and electron density distribution for MIL-53(Fe) remains unexplored. And the specific investigations on TC degradation pathway with S-MIL-53(Fe) is also deserve further attentions.

In this work, we reported the intramolecular sulfur modified MIL-53 (Fe) of S3-MIL-53(Fe) with regular spindle-shaped polyhedron morphology. The newly synthesized S3-MIL-53(Fe) exhibited high improved practical performance and obviously competitive edge. Both experimental and theoretical simulation was probed to describe the intramolecular scale modulation way and the origin of this enhanced activity. The intermediate energy level was also proved to be induced by the formation of Fe-S-C bridges in S-MIL-53(Fe) with partially replacing O atoms during the thermal reaction process for the first time. Thereby, this work opens a new research doorway in tuning the photocatalytic activity for iron-based metal organic framework family.

2. Materials and methods

2.1. Materials

1,4-Benzenedicarboxylic acid (H$_2$BDC, 99%), Ethylene glycol (EG, 99.5%), N,N-dimethylformamide (DMF, 99%) and sublimated sulfur were obtained from Sinopharm Chemical Reagent Co., Ltd (Shanghai, China). Tetracycline (TC), Iron (III) chloride hexahydrate (FeCl$_3$•6H$_2$O, 99%), (> 250 U/mg), ethylenediaminetetraacetic (EDTA), isopropanol (IPA, 99%) and p-benzoquinone (BQ) were purchased from Macklin Chemical Reagent Co., Ltd (Shanghai, China). All the chemical reagents were provided by commercial suppliers with analytical purity or higher.

2.2. Synthesis of the photocatalysts

2.2.1. Synthesis of MIL-53(Fe)

An improved solvothermal method similarly to the reported literature was applied to fabricate the MIL-53(Fe) [12]. The detailed synthesis procedure was described in the Supporting Information (Text S1).

2.2.2. Synthesis of S-MIL-53(Fe)

The S-MIL-53(Fe) was prepared through a vacuum heating method as described above. In the typical thermal synthesis process, different amount of sublimed sulfur was sealed with the as-prepared MIL-53(Fe) in a quartz tube and heated to 350 ℃ under vacuum until the sulfur was intramolecular incorporated into MIL-53(Fe).

2.3. The photocatalytic performance evaluation

The photocatalytic activity was identified through the TC degradation under visible light irradiation (λ > 420 nm) after adsorption procedure. The visible light was simulated by a 300 W Xenon lamp with a 420 nm cutoff filter. The photocatalytic reactor was constantly located at 20 cm far away from the Xenon lamp. In a typical photocatalytic activity test process, 10 mg of the S-MIL-53(Fe) was dispersed into 100 mL TC aqueous solution. The initial concentration of TC was 50 mg/L. Before the irradiating process, the suspension was stirred in dark for 1 h under open air environment at room temperature to achieve adsorption and desorption equilibrium. About 4 mL of suspension was withdrawn regularly and filtered through 0.22 μm PTFE syringe filters before analysis. The concentrations of TC were monitored by an Ultraviolet spectrophotometer (UV-2600, SHIMADZU Corporation, Japan). Liquid Chromatograph Mass Spectrometer (LC-MS/MS) (1290/6470 Triple Quad, Agilent) system was used to analyze the detailed degradation information. Elution was conducted at a flow rate of 0.2 mL/min with H$_2$O containing 0.1% (v/v) formic acid as eluent A and acetonitrile as eluent B. The column temperature was set at 30 °C and the injected volume maintained 5 μL. The mass range of MS was scanned from 100 to 600 *m/z*. The quantum efficiency and space time yield was also calculated to evaluated the photocatalytic performance of the as-synthesized catalyst and the detailed calculation process was presented in Supplementary Information (Text S6 and Text S7).

To identify the activity specials of S-MIL-53(Fe) during the photocatalytic TC degradation process, different scavengers were added to the control experiments. Among those scavengers, EDTA, IPA and BQ are scavenging agents for the photogenerated hole (h$^+$), hydroxyl radical (•OH), and superoxide iron radical (•O$_2^-$), respectively [2,3]. About 1 mM/L scavenger was added before the light irradiation with other experimental conditions maintained. The catalyst sample was attentively collected with the washing and drying process for the recycling tests after the photocatalytic reaction.

2.4. Characterization and computational details

The detailed properties characterization and computational calculations were presented in Supplementary Information.

3. Results and discussion

3.1. Structural description

The synthesis pathway for the sulfur incorporated into MIL-53(Fe) is illustrated in Scheme 1. The prepared MIL-53(Fe) was mixed with sulfur after constant grinding. The sulfur species was first adsorbed within the evacuated MIL-53(Fe) and then formed the corresponding complexes by a thermal induced process. To verify the microscopic morphology of the S3-MIL-53(Fe), SEM, TEM, and HTEM measurements were performed. As displayed in Fig. 1(a-b), the MIL-53(Fe) particle exhibits a regular spindle-shaped hexagon morphology with a smooth surface. Compared to the previously reported structures, the obtained MIL-53(Fe) in this work possesses a shorter size at the middle length direction of the spindle resulting in a more exposed surface [21]. After the annealing process to incorporate sulfur, the morphology structural and the homogeneity of MIL-53(Fe) were not altered. Some irregular protrusions on its surface can be observed indicating that the introduction of sulfur particles has a rare effect on the morphology (shown in Fig. 1c). TEM images in Fig. 1d also confirm the regular spindle-shaped composite and surface roughness. HTEM images in Fig. 1(d) further illustrate the successful synthesized crystallized S-MIL-53(Fe) catalyst with a regular structure. The elemental mapping analyses in Fig. 1f show that the elements of Fe, C, O and S are well-distributed all over the whole S-MIL-53 (Fe) sample, indicating that the sulfur was homogeneously introduced into the MIL-53(Fe).

The phase structure was identified through XRD, as shown in Fig. 2a, the MIL-53(Fe) presents characteristic peaks at 9.26°, 12.42°, 17.5° and 25.1° which are well corresponding to the reported results, indicating the successful fabrication of MIL-53(Fe) [12]. There is no obvious new
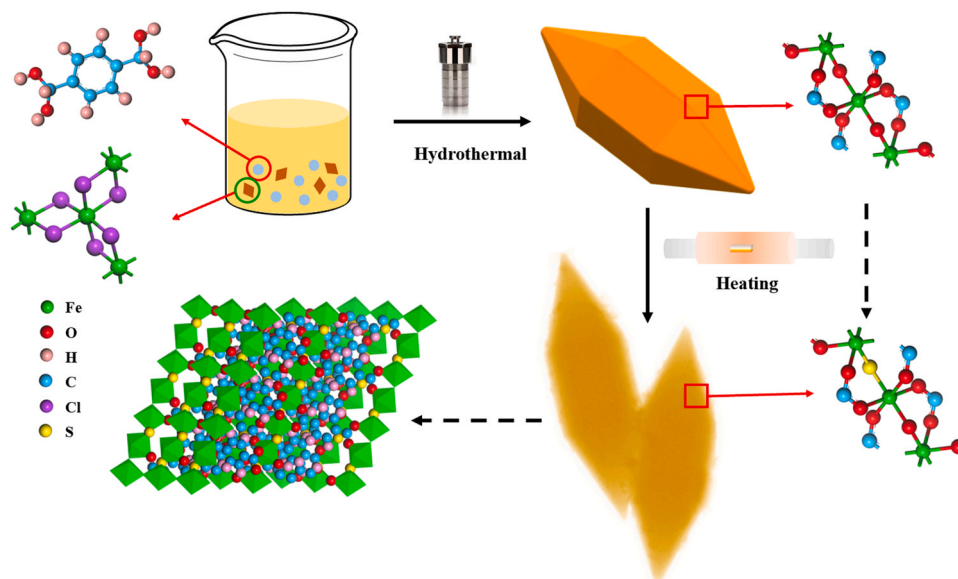
Scheme 1. Illustration of fabrication and sulfur intramolecular modulation regular spindle shaped iron-based metal organic framework.

character peak in XRD patterns of S-MIL-53(Fe) suggesting that introducing sulfur into MIL-53(Fe) particles does not alter the crystal phase structure. This phenomenon indicates incorporation of sulfur might be achieved through replacing partial atoms in MIL-53(Fe) framework [22]. Moreover, it is notable that the characteristic peaks at 17.5 (Fig. 2b) displayed a slight shift to higher angles after sulfur modification, which implies that incorporation of sulfur into MIL-53(Fe) framework will lead to lattice distortion. Fourier Transform infrared spectrometer spectrums (Fig. 2d) are also obtained to identify the molecular structures and functional groups in pure MIL-53(Fe) and S-MIL-53(Fe) composites. As displayed in Fig. 2d, there is a broad band in the region between 3000 and 3500 cm^{-1} for both MIL-53(Fe) and S3-MIL-53(Fe) which can be attributed to the residual water originated from the hydrothermal preparing process and the adsorbed air moisture [23]. The strong band at around 1678 cm^{-1} is corresponding to the stretching vibration of C=O bands [24]. The obvious peaks at around 1394 and 1622 cm^{-1} are possibly originated from the carboxyl groups symmetric and asymmetric vibrations which certificates the dicarboxylate linker in both MIL-53(Fe) and S-MIL-53(Fe) [25]. The absorption band at 571 cm^{-1} is related to the Fe—O bonds stretching vibration, indicating that the Fe-oxo cluster exists between the carboxylic group and inorganic metal [26]. The emerging peaks at 570–670 cm^{-1} can be attributed to the band formation of -C-S- implying the sulfur incorporating in the S-MIL-53(Fe) [27]. Moreover, the strong bands at 800–900 cm^{-1} further indicate the formation of a new sulfur-based bond in S-MIL-53(Fe). Those results suggest that the ways of sulfur incorporating in S-MIL-53(Fe) is through intramolecular modification. The chemical valence state and surface chemical compositions of MIL-53 (Fe) and S-MIL-53(Fe) are further analyzed by the XPS. As displayed in Fig. 3, the XPS survey spectra of MIL-53(Fe) consist of strong peaks of Fe, O and C elements while the S-MIL-53(Fe) is composed of strong peaks including Fe, S, O and C elements. The presented strong peak of S reveals the sulfur composition on S-MIL-53(Fe). As represented in the high-resolution of Fe 2p spectrum (Fig. 3a), the binding energies at 728.3 and 709.8 eV can be attributed to the formation of an iron-based band with sulfur in S-MIL-53(Fe) which confirms the successful intramolecular modulation related to iron bonding [28]. The peaks at 724.6, 717.2 and 712.3 eV shift to lower energy compared to that in pure MIL-53(Fe) suggesting the negative charges by the introduced sulfur. Characteristic peaks of MIL-53(Fe) in Fig. 3c located at 532.3 and 531.6 eV in the O 1s high-resolution XPS spectra are assigned to C=O and C—O respectively [29]. Similarly, the O 1s peaks also shift to lower

binding energies due to the enhanced electron transfer derived from the sulfur modulation on MIL-53(Fe) framework [30]. As shown in Fig. 3b, the high-resolution of the C 1s spectrum for pure MIL-53(Fe) could be deconvoluted into two peaks while the three peaks can be observed in S-MIL-53(Fe). The emergence of a characteristic peak centered at about 287.3 eV also demonstrates the combination of carbon with sulfur and suggesting that sulfur most probably replaces oxygen atom formatting the C—S bonds [31]. The peak deconvoluting into two peaks centered at the binding energy of 161.4 and 163.7 eV are assigned to sulfur further confirming the chemically bonded sulfur moieties in the S-MIL-53(Fe) (Fig. 3a) [32]. Therefore, the powder XRD patterns, FTIR spectrum and XPS survey spectra analysis clearly confirm the successful synthesis of intramolecularly modulated iron-based metal organic framework with sulfur.

N$_2$ adsorption-desorption isotherms were also recorded to investigate the specific surface area and internal pore structure for the obtained samples. As displayed in Fig. 2(e), the MIL-53(Fe) is represented by the type IV isotherm indicating the typical feature of mesoporous materials [21]. The BET of the different composite materials is approximately 8.68 m^2/g, 13.65 m^2/g, 56.95 m^2/g, 95.14 m^2/g and 113.74 m^2/g respectively (Table. S2). The increased BET can be attributed to the modification of the pore structure of the MIL-53(Fe) by embedding sulfur. Constantly, the MIL-53 (Fe) can reversibly adapt its pore size from a closed form to an open form which depending on the guest molecule and reaction temperature. And according to the preparation process of in our work, the since through one-pot method leads to an open form MIL-53 (Fe). When heating at 200 °C, the neutral terephthalic acid in open form MIL-53 (Fe) will leave the structure and creating an open and larger pore size MIL-53 (Fe) [14]. After cooling to normal atmospheric temperature, a more closed form was formatted resulting the sulfur particles entering the pore structure [23]. The larger specific surface area was beneficial for providing more activated sites on the catalyst surface resulting in improved photocatalytic performance.

3.2. Practical photocatalytic performance investigations

Based on the afore-mentioned results, the photocatalytic performance of the as-synthesized catalysts by conducting TC degradation under visible light were evaluated. To achieve the adsorption and desorption equilibrium, the samples were stirred for an hour under dark conditions. As displayed in Fig. 4a, the TC solution concentration shows scarcely changes in the absence of photocatalysts during the test period.
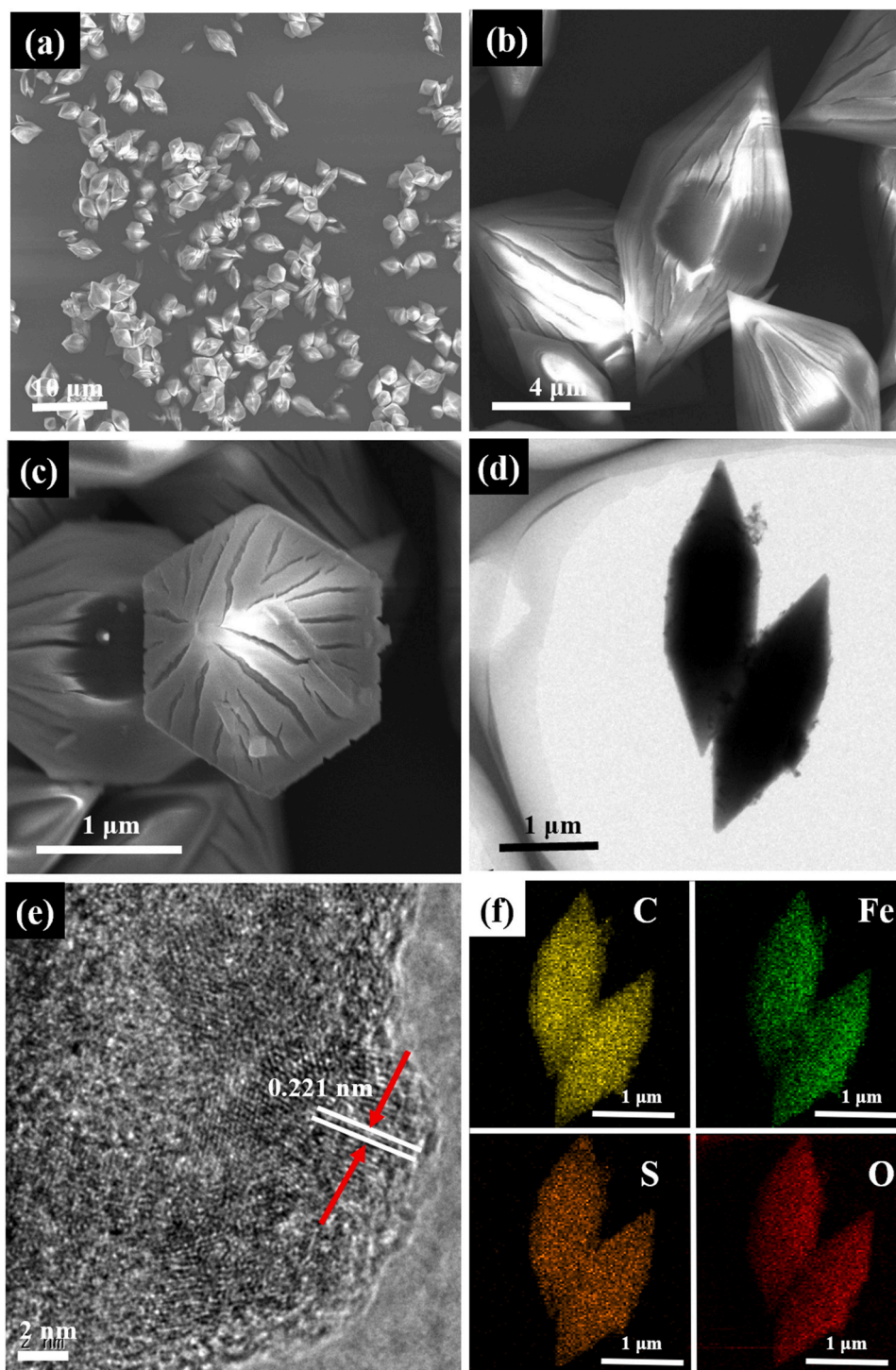
Fig. 1. (a-b) TEM image of MIL-53(Fe). (c) SEM image of S-MIL-53(Fe). (d) TEM image of S-MIL-53(Fe). (e) HTEM image of S-MIL-53(Fe). (f) Elemental mapping images.

The S3-MIL-53(Fe) catalyst exhibits higher adsorption capacity comparing with the pure MIL-(Fe) sample. After 60 min visible light irradiation, the TC removal efficiency reached 96.8% when the S3-MIL-53(Fe) catalyst was employed, while the pure MIL-53(Fe) induced much lower degradation of 23% at the same irradiation condition. In addition, the photocatalysis experiment of sublimed sulfur and the mixed sample by grounding sublimed sulfur with MIL-53(Fe) samples (1:1) for tetra-cycline (TC) degradation were also conducted and the results are shown in Fig. S6. As it shown, the sublimed sulfur exhibited negligible TC degradation efficiency and the mixed sample also displayed low TC

degradation efficiency. Therefore, the observed increasing in rate came from the modified S3-MIL-53(Fe). To specifically evaluate the photo-catalytic performance of the S3-MIL-53(Fe), the reaction kinetic rate, apparent quantum efficiency and STY were calculated (seen in Text S6) and the results are shown in Table S5. As it depicted, the kinetic rate for S3-MIL-53(Fe) is 1.088 mmol/g/h which is about five times that of pure MIL-53(Fe) (0.239 mmol/g/h). The AQE for S3-MIL-53(Fe) is 27.82% which is over 30 times than that of pure MIL-53(Fe) (0.903%). These results indicate that the intramolecular sulfur modification in our work is an effective way to improve the photocatalytic performance of MIL-53
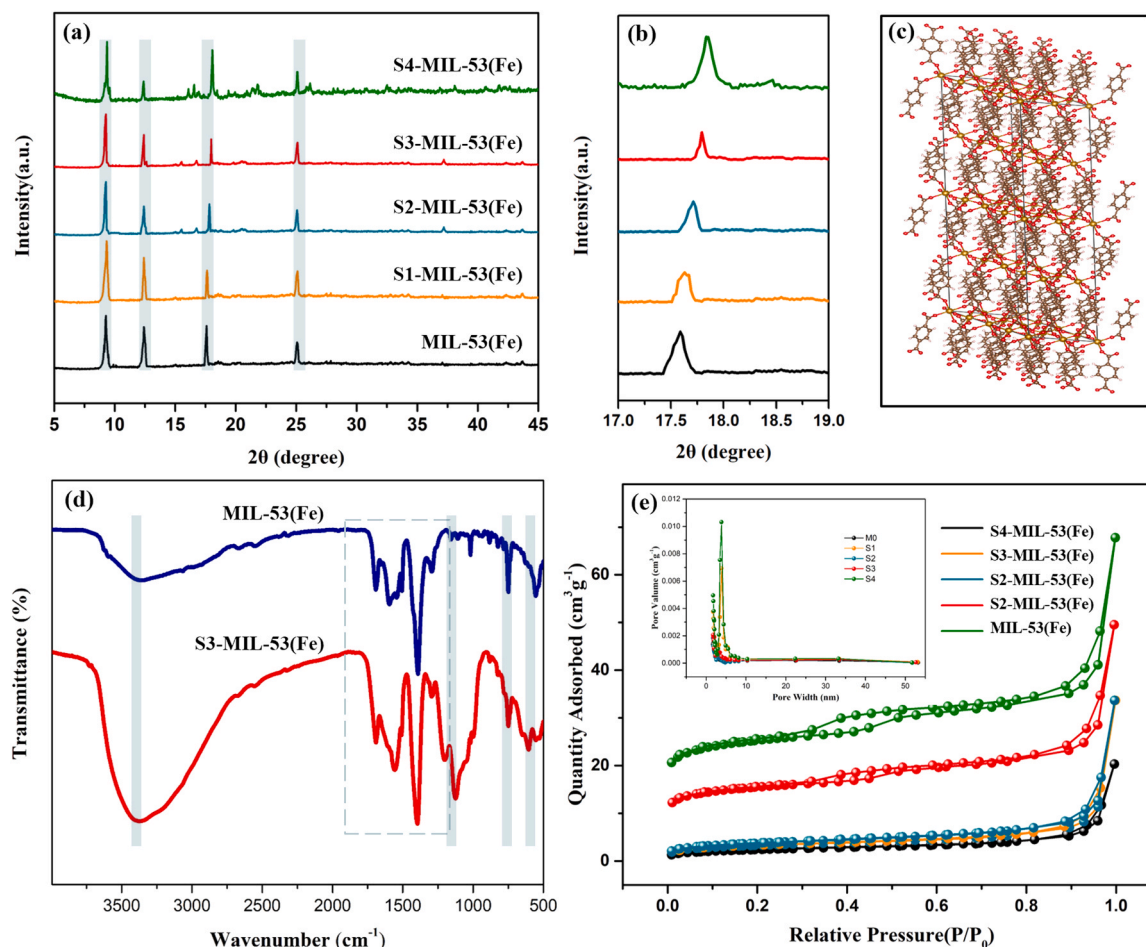
Fig. 2. (a) and (b) XRD patterns (c) model structure and (d) FT-IR spectra of as-prepared MIL-53(Fe) and S-MIL-53(Fe) samples, (e) N₂ adsorption and desorption. isotherms, insert showing the corresponding pore size distributions for the as-prepared catalysts.

(Fe). Furthermore, the S3-MIL-53(Fe) has a reaction kinetic rate of 1.088 mmol/g/h, which is much higher than that of other MOF based photocatalyst for TC degradation efficiency (from Table. S4). It could also be noticed that further rich the sulfur content into MIL-53(Fe) however decreased the TC degradation rate. This result is caused by over captured photo-induced carriers at the trapping center arising from the redox cycle system with over-rich sulfur incorporating [33]. Therefore, the properly introduced sulfur content of the S3-MIL-53(Fe) sample exhibits the best photocatalytic performance for TC photo-degradation. The pseudo-first-order kinetic equation was used to fit the photocatalytic oxidation kinetic curves of $ln (C/C_0)$ as depicted in Fig. 4 (b). The equation is expressed as $ln (C/C_0) = -kt$, where C/C_0, k and t corresponded elative concentration of residual TC, the apparent reaction rate constant and the irradiation time [34]. In Fig. 4, the kinetic rate constant for S-MIL-53(Fe) is much greater than that of the pure MIL-53 (Fe), indicating that the formation of Fe-S-C under intramolecular encapsulating sulfur played a significant role in enhancing the photo-degradation kinetics. The results further confirm that intramolecular modulating MIL-53(Fe) with sulfur could efficiently improve the pho-tocatalytic activity. It is well known that both the chain of photocatalytic oxidation reaction and the formation of radical species will be signifi-cantly affected by the pH of the water environment [35]. Therefore, the pH values were adjusted from 3 to 10 through controlling the HCl (0.1 M) or NaOH (0.1 M) addition amount to investigate the impact of the pH conditions on TC photodegradation. As exhibited in Fig. 4(d), the pH value markedly affects TC adsorption under dark conditions. When decreasing pH value down to acidic conditions, the TC adsorption of S3-MIL-53(Fe) sample is increased, possibly stemming from the cation

exchanging process [36]. The TC adsorption of S3-MIL-53(Fe) is decreased under alkaline conditions due to the repulsive electrostatic force between two negatively charged molecules. The pH condition also shows extent influence on the photocatalytic degradation efficiency of TC under visible light irradiation. Therefore, in this research, the su-preme performance of pH value was set at 6. The practicability of the S3-MIL-53(Fe) catalyst was further confined through investigating the TC photodegradation performance in real water environment including river and lake water. As displayed in Fig. 4e, the S3-MIL-53(Fe) exhibits great TC photodegradation performance as before in river water envi-ronment indicating its promising practicability. It is also noticed that the photocatalytic degradation efficiency of TC in tap water is lower than that in deionized water and river water. The basic characteristics of river water and tap water are presented in Table S6. As it shown, the con-centration of Cl⁻ in tap water is obviously higher than that of the river water. It has been demonstrated that anion of Cl⁻ could scavenge •OH to generate Cl• [37]. Thereby, the higher concentration of Cl⁻ in tap water might be the main inhibition effect factor for the decreased TC removal efficiency. This result is also consistent with the reported literatures [38]. The kinetics study was also conducted and the results were depicted in Fig. 4f. The corresponding k values in both river and lake water were lower than that in simulated wastewater, which may be related to the complex components in real samples. The reusability and stability were also the recognized indicators to assess the practicability of the synthesized catalyst [39]. Therefore, the practical application value of S3-MIL-53(Fe) was evaluated by repeating the TC photo-degradation experiment for five times. Before each circle, the catalyst was centrifugated, washed and dried for collection. As can be seen in
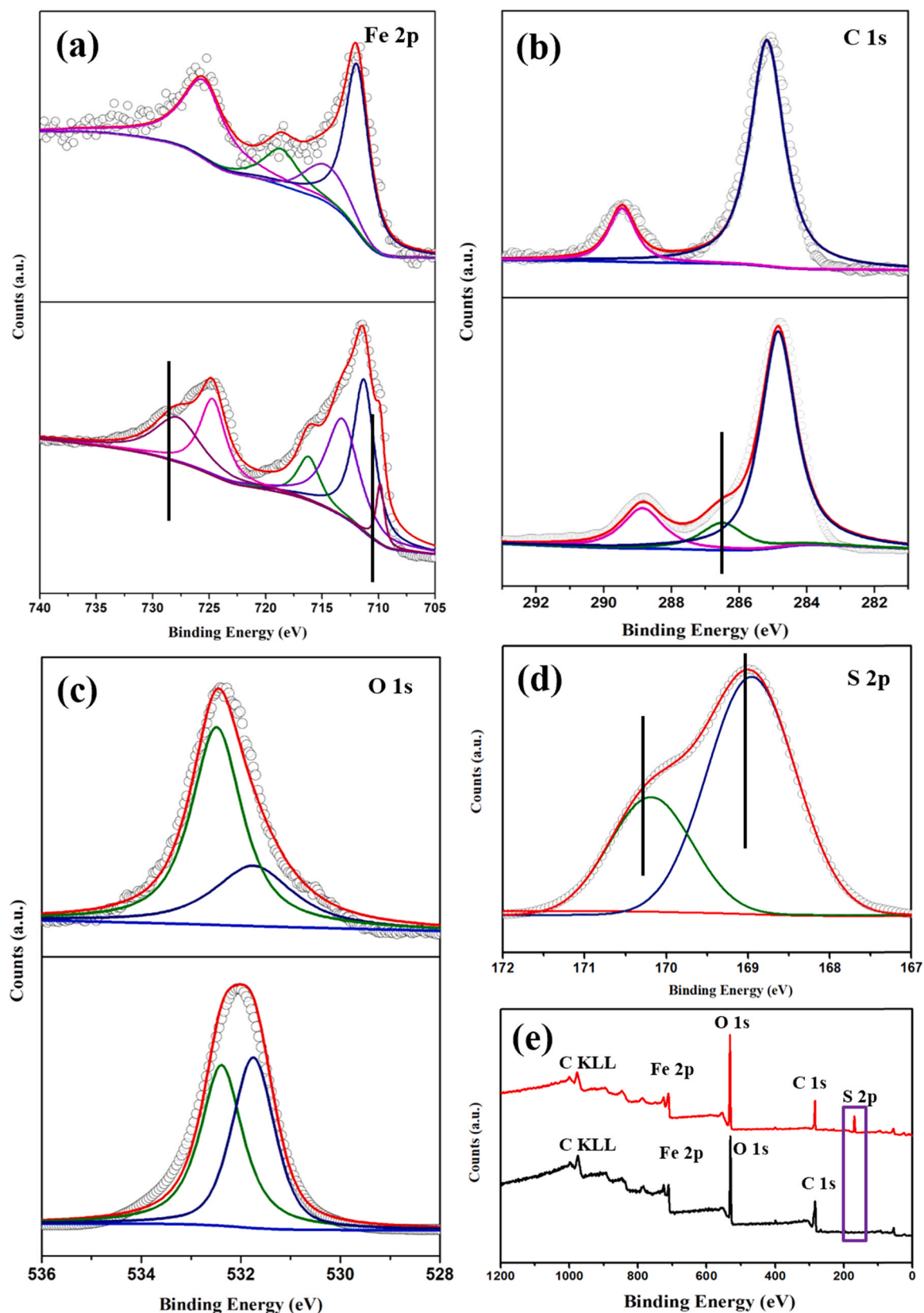
Fig. 3. Representative high-resolution XPS spectra of MIL-53 (Fe) and S-MIL-53 (Fe): (a) Fe 2p, (b) C 1s, (c) O 1s, (d) S 2p, and (e) full spectrum.
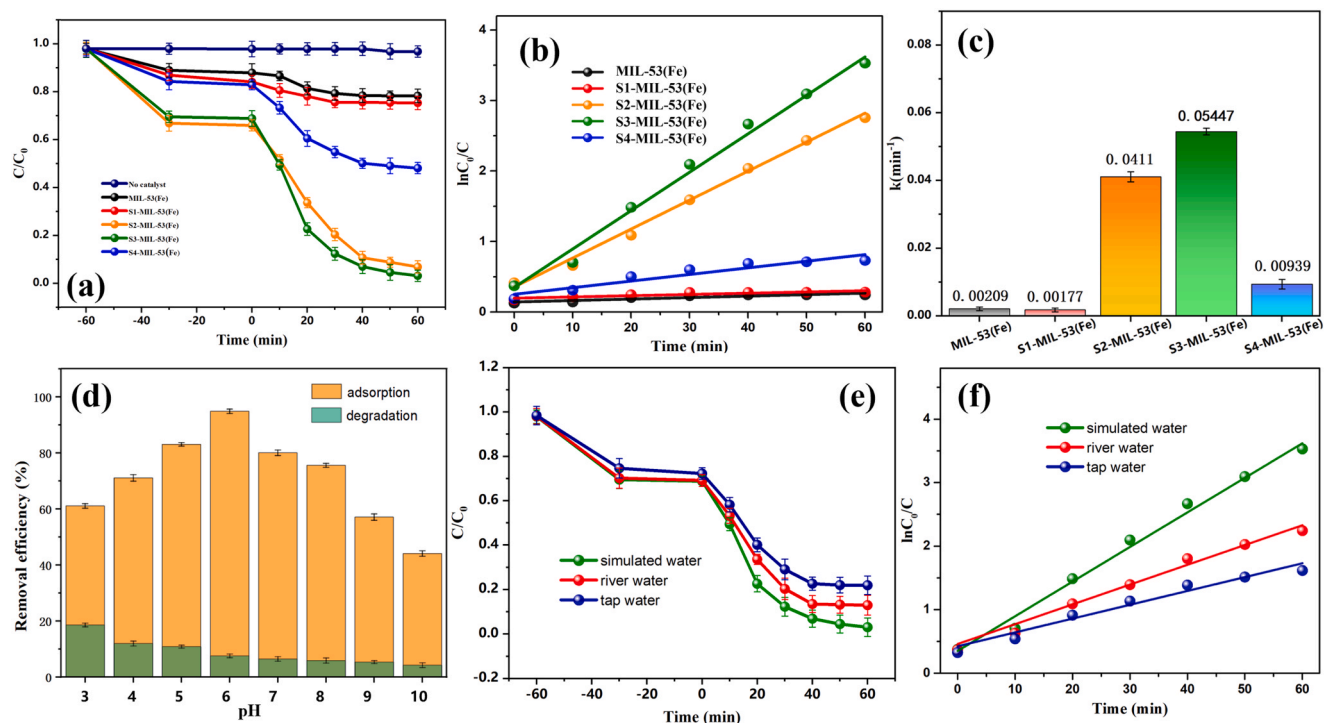
Fig. 4. (a) Effects of radical catalysts (conditions: solution volume = 100 mL, catalyst = 10 mg, pH = 6, TC = 50 mg/L). (b) the pseudo-first-order kinetics. (c) the corresponding calculated k value. (d) effects of pH on TC degradation. (e) the photocatalytic degradation of TC using S3-MIL-53(Fe) in river water and tap water. (f) the corresponding pseudo-first-order kinetics.

Fig. S3, the photocatalytic efficiency of S3-MIL-53(Fe) for TC degradation maintains over 95% even after several repeated cycling tests indicating its high stable efficiency. Moreover, the phase compositions of MIL-53(Fe) and S3-MIL-53(Fe) after the repeated cycling test were also examined through the XRD diffraction patterns (in Fig. S4). The crystal structure shows no obvious change after five cycles. The micromorphology of the catalyst after the cycling test was also characterized through SEM which exhibits negligible changes (shown in Fig. S3). Moreover, the leaching concentration of Fe was conducted on an inductively coupled plasma mass spectrometer (7900) and three parallels were tested for each sample to avoid systematic error. Before the leaching test, the standard curve was built (shown in Fig. S9b) and the results of Fe leaching concentration are displayed in Fig. S9a. The initial tested leaching concentration of Fe for MIL-53(Fe) and S3-MIL-53(Fe) is about 349.9 and 250.4 ppb (10–3 mg/L) respectively. After the photocatalytic process, the leaching concentration of Fe for both MIL-53(Fe) and S3-MIL-53(Fe) do not exhibits significant increasing which indicates the favorable water stability. Besides, the tested leaching concentration of Fe for S3-MIL-53(Fe) is obviously lower than that of the pure synthesized MIL-53(Fe) demonstrating that the heating treating under vacuum condition can favor its water stability. Thereby, S3-MIL-53(Fe) catalyst was proved to possess high reusability and stability during the TC photocatalytic process confirming the promising potential for practical application.

Subsequently, radical trapping experiments were carried out to determine the main active species related to TC removal by S3-MIL-53 (Fe) photocatalytic degradation system. Noticeably, with the addition of BQ as $\bullet O_2^-$ scavenger into the reaction conditions, the degradation is remarkably reduced over 30% (Fig. S5), suggesting that $\bullet O_2^-$ is one of the crucial active species in this reaction system. Similarly, when EDTA was employed as a scavenger, the photodegradation efficiency is immensely decreased, verifying that the photogenerated h^+ is the other active species during the TC degradation process. The TC degradation efficiency is also minorly decreased with the presence of IPA. The existence of reactive species was qualitatively tested through the electron

spin resonance (ESR) spin-trap technology [18]. As shown in Fig. 5g, there are strong characteristic signals of DMPO-$\bullet OH$ after 5 min light irradiation, suggesting the accumulated amounts of $\bullet OH$. Meanwhile, the DMPO-$\bullet O_2^-$ also exhibits strong peak intensity indicating the existence of $\bullet O_2^-$ in the reaction system. Therefore, the most responsible active specie for the photocatalytic degradation process in this system is $\bullet O_2^-$ which provided proof for the photocatalytic mechanistic analysis.

3.3. Photoelectric properties determination

Based on the above results, the optical and electrical properties of the catalysts were analyzed to clarify the reasons for the enhanced photoactivity. The photo-absorption behavior of the catalysts was investigated through UV–vis diffuse reflectance measurement [40]. As presented in Fig. 5(a), the pure MIL-53(Fe) sample exhibits strong optical absorption with an absorption edge at around 600 nm while the S3-MIL-53(Fe) catalyst shows an extended absorption edge over 650 nm. This implies that the as-synthesized catalyst samples present a commendable visible light response. Moreover, the S3-MIL-53(Fe) displays higher optical absorption intensity in comparison with pure MIL-53(Fe) under the visible light region. It has been proven that the visible light response of MIL-53(Fe) could be attributed to the multiple metal ions active sites and excitation of the conjugated coordination bonds [41]. To acquire the band-gap, the formulation of $\alpha h v = A(h v - Eg)^n$ was conducted, in which Eg presents the energy band-gap, h presents Planck's constant, α presents absorption coefficient, v corresponds to light frequency, and n presents the characteristics for the transition semiconductors [42]. As shown in Fig. 5b, the corresponding band gaps for pure MIL-53(Fe) and S3-MIL-53 (Fe) are 2.63 eV and 1.74 eV respectively, suggesting that the incorporated sulfur has a great effect on the electronic structure. Followed by, Mott-Schottky plots were employed to investigate the exact band-edge positions of S3-MIL-53(Fe) in Fig. 5c. The flat-band potentials (E_{fb}) of pure MIL-53(Fe) and S3-MIL-53(Fe) were determined by 100, 500, 1000 Hz which corresponding to the value of − 0.17 and − 0.38 V versus SCE [43]. As the Mott-Schottky plots for S3-MIL-53(Fe) displayed
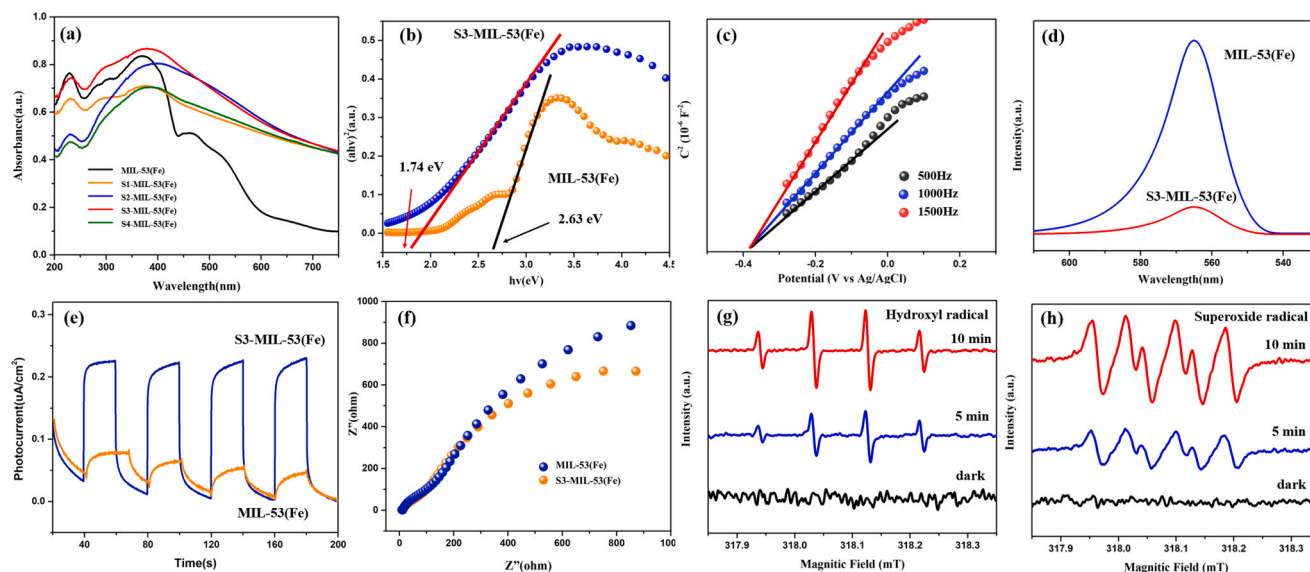
Fig. 5. (a) The UV–Vis DRS spectra. (b) the corresponding band gaps. (c) Mott-Schottky plots. (d) The PL spectra. (e) and (f) Transient photocurrent plots and electrochemical impedance spectra. (g) and (h) The ESR spectra of DMPO-·O^{2-} and DMPO-·OH- in the presence of S3-MIL-53(Fe) under dark and visible light irradiation.

a positive slope linear region implying the n-type nature of the catalyst, the saturated calomel electrode potential (E_{SCE}) value is added 0.24 to equals the normal hydrogen electrode potential (E_{NHE}). Therefore, the E_{fb} for S3-MIL-53(Fe) is equal to -0.14 eV versus NHE [44]. The valence band (VB) edge potential for S3-MIL-53(Fe) is calculated to be $+1.6$ eV by the empirical formula $E_{VB} = E_{CB} + E_g$. The PL spectra for S3-MIL-53(Fe) exhibits distinctly depressed emission compared to pure MIL-53(Fe) indicating a more efficient transfer of photogenerated electrons and holes (shown in Fig. 5d). To further demonstrate the result, electrochemical analyses were also conducted. The photogenerated charge separation efficiency of the pure MIL-53(Fe) and S3-MIL-53(Fe) photocatalysts is assessed through the investigation of transient photocurrent responses. Several light/dark irradiation cycles were measured and the results are presented in Fig. 5e. The photocurrent is increased rapidly under the visible light irradiation and speedily returned to zero in the dark. Much higher photocurrent intensity is observed in the S3-MIL-53(Fe) sample indicating an improvement of charge carrier separation efficiency after the sulfur modulation process (shown in Fig. S7) [45]. Positive effect of the sulfur incorporation on the charge carrier separation has also been reported previously [14,22,23]. Meanwhile, the retention of current intensity under several light/dark cycles by light irradiation revealed that the S3-MIL-53(Fe) exhibited superior stability during photocatalytic test. Commonly, the electronic conductivity of the obtained samples could be expressed by the diameter of semicircle arc in EIS Nyquist plots and a smaller semicircular arc diameter implied a higher charge transfer rate [46]. As displayed in Fig. 5f, smaller semicircular arc diameter for the S3-MIL-53(Fe) than the MIL-53(Fe) indicate a faster charge transfer rate and longer lifetime of charge carriers. In addition, charge transfer resistance could be reduced with the introduction of the sulfur into MIL-53(Fe) resulting in the enhanced photocatalytic activity. In short, these results firmly demonstrated that the intramolecular modulation MIL-53(Fe) with sulfur is a promising strategy to improve the photocatalytic performance.

3.4. Theoretical exploration

To further reveal the intramolecular sulfur modulation mechanism for the enhanced photocatalytic performances, the band structure and energy level of MIL-53(Fe) and S-MIL-53(Fe) were investigated by conducting the density functional theory (DFT) calculations over the

Vienna ab initio Simulation Package (VASP) [47]. Fig. 6a-b shows the optimized geometric structures for MIL-53(Fe) and S-MIL-53(Fe) respectively., The calculated band-gap of MIL-53(Fe) is 2.27 eV which has a tolerable deviation (shown in Fig. 6c). The S-MIL-53(Fe) exhibited a lower band gap and this result is consistent with the UV–vis spectra. To better illustrate the role of each element, the total and partial density of states (DOS) were also calculated. As depicted in Fig. 6c and Fig. 6d, comparing with MIL-53(Fe) both the conduction band and valence band for S-MIL-53(Fe) shifts to higher energy levels suggesting the electronic modulation with intramolecular incorporating sulfur. Specifically, below the conduction band (CB), a middle energy level at 1.21 eV can be observed in the band-gap structure of S3-MIL-53(Fe). The emerging intermediate energy level in S3-MIL-53(Fe) could be attributed to the charge-transfer transition on Fe-S-O bridges and further evidencing the incorporation of the sulfur atom into the framework through intramolecular modification. And under the visible light irradiation, the photoexcited electrons could easily jump up to the middle energy level from valence band inducing S3-MIL-53(Fe) with superior photocatalytic performance with this facilitated the electronic excitation [48]. To better illustrate the electronic transition, the charge distributions are also presented in Fig. 6e. Both MIL-53(Fe) and S-MIL-53(Fe) show electron accumulation at the framework forming a substantial charge distribution when seeing from the top-view of differential charge density in fully relaxed structures. Comparing to pure MIL-53(Fe), the electron redistribution in S-MIL-53(Fe) exhibits a strong interaction on the bridge of Fe-S-C providing faster electron transfer. The substituted sulfur provided the capability to increase the benzene ring electron density which enlarged the conjugation of the coordination bonds, leading to the extension of the light absorption at the visible region [49]. This result is also supported by the UV–vis spectra (Fig. 5a). The electron accumulation originating from the electron transfer is favorable for photoactivity enhancing and increasing the affinity for the OH- reactants. Furthermore, the pronounced charge distribution in the S-MIL-53(Fe) also provided a remarkable electronic coupling effect, leading to higher photoactivity.

3.5. Proposed photocatalytic mechanism and degradation pathway

Based on experimental and calculated results, a photocatalytic mechanism illustrating the high-efficiency photocatalytic degradation
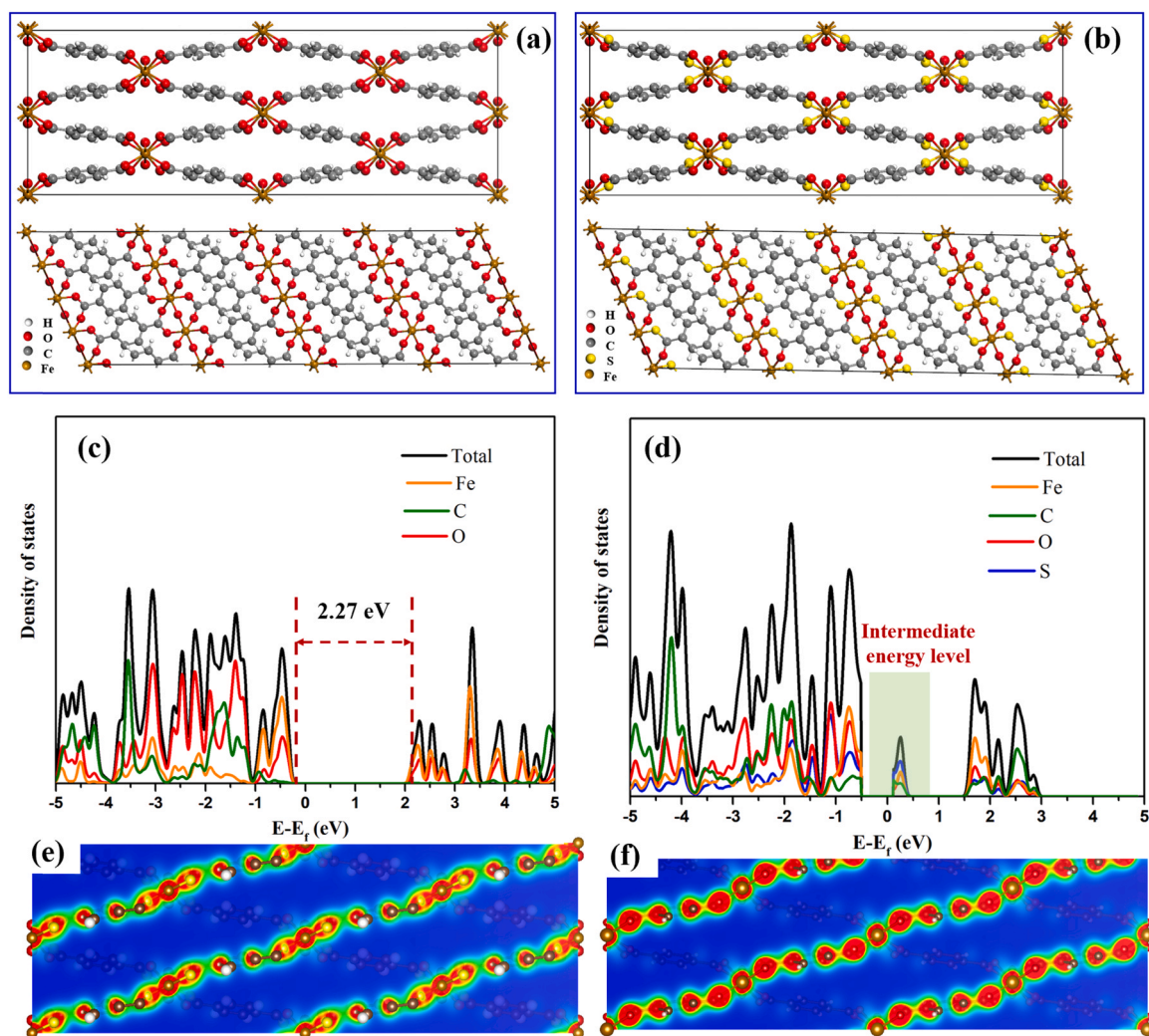
Fig. 6. Density functional theory simulation. (a) and (b) Optimized structure of MIL-53(Fe) and S3-MIL-53(Fe). The position of Fermi level is set to be 0 eV. (c) and (d) PDOS and TDOS of MIL-53(Fe) and S3-MIL-53(Fe). The simulated electron-density difference of (e) MIL-53(Fe) and (f) S3-MIL-53(Fe).

of TC over S3-MIL-53(Fe) was proposed in Fig. 7. The MIL-53(Fe) was intramolecularly modulated by sulfur thereby emerging an intermediate energy level. More incoming light was used with the intermediate energy level and enhanced the charge separation through the modulated structure leading to improved photocatalytic activities for S3-MIL-53 (Fe). Meanwhile, as explained in Fig. 7, the CB potentials and corresponding VB potentials of S3-MIL-53(Fe) were calculated to be − 0.14 eV and + 1. 6 eV, respectively. The photo-produced electrons on the CB could migrate to both the intermediate energy level and CB of S3-MIL-53(Fe). Therefore, the electrons were effectively photoexcited to different energy levels, producing more electron-holes. The carbon-based frameworks in MIL-53(Fe) were constantly acted as an electron conductor to separate the electron-hole and transmit the electron to the conduction band [50]. After the sulfur modulation, the electrons in S3-MIL-53(Fe) are suggested to transfer along with the Fe-S-O bridges which are verified by the results of the differential charge density map. The Fe-S-O bridges provided with conductive electron transport "highway" which speeding up the electron transmission resulting in better charge separation. As the CB potentials of S3-MIL-53(Fe) is more negative than the reduction potential of $O_2/\bullet O_2^-$ (−0.046 eV vs. NHE), the molecule oxygen can be reduced to produce $\bullet O_2^-$ for TC degradation by the accumulated electrons on the CB of S3-MIL-53(Fe). Coincidently, the above result well demonstrated that the $\bullet O_2^-$ generated on the surface of S3-MIL-53(Fe) was the most main reactive species, which could attack the adsorbed TC molecules as quickly as possible. Consequently,

the photocatalytic activity was promoted through the ingenious cooperation between charge transfer steering and active site enriching. Therefore, the S3-MIL-53(Fe) has the advantages of enhancing light absorption, enlarge contact area, and accelerating charge separation and transport. The photogenerated electron-hole pairs were favorited to migrate and separate on S3-MIL-53(Fe) with intramolecular modulated sulfur, and leading to efficient photocatalytic performance for organic waste water treatment.

The TC degradation process on S3-MIL-53(Fe) was specifically investigated to lead further insight into the photocatalytic mechanism. The degradation intermediates at different reaction times were detected by the LC-MS technique (Figs. S11–13). Based on the predicted reactive sites and identified degradation intermediates, the possible TC degradation pathways were proposed (Fig. 8). The dominant peak at 445.1 can be ascribed to the original TC (Fig. S10) [4]. Generally, the N-methyl, double bond, aromatic ring, ketone group and amino group are frequently reactive sites. The degradation pathways of TC was mainly including specific functional groups cleavage and ring-opening reactions [51]. As depicted in Fig. 8, the hydroxyl group is initially tended to attack unsaturated carbon bonds (C═C) on TC (with $m/z = 445.1$), and forming the C_1 ($m/z = 461.1$). Afterward, with the increased positive point charges caused by the hydroxylation process, the n-demethylation and dehydration reaction were promoted by superoxide radical attack resulting in the C_2 ($m/z = 398.1$). The additional electron at the ketone position realized the deamidation process, leading
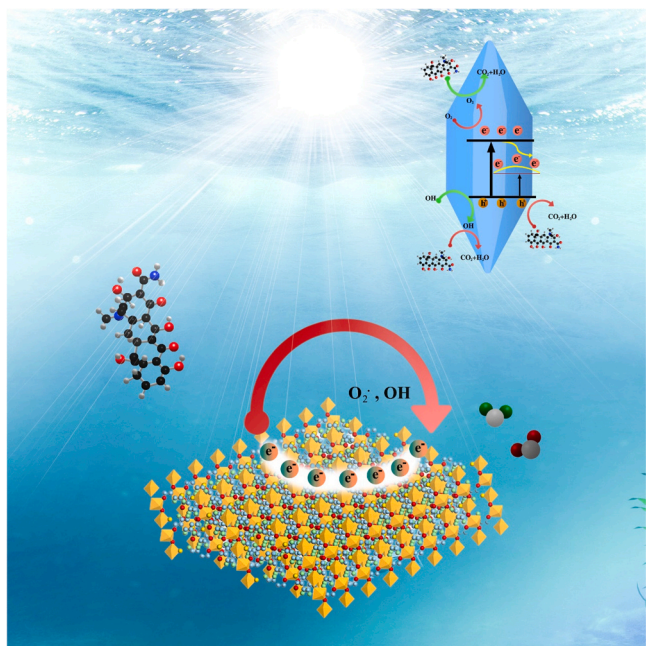
Fig. 7. Schematic diagram of the system working procedure. Step 1: the TC are stored in the frameworks of the S3-MIL-53(Fe) material; Step 2: S-MIL-53(Fe) act as photocatalysts, and the stored TC are degraded into CO_2 and H_2O under solar illumination.

to the generation of C_3 ($m/z = 308.1$). Similarly, the original TC can be transformed directly via the demethylation, deamidation and hydroxylation process. After losing the amido group, methyl group, and the deamidation, C_4 with $m/z = 415.2$ was detected. With a ketone group oxidation and deamination process, C_5 ($m/z = 367.1$) was generated. The TC transforms to C_6 ($m/z = 429.1$) via the demethylation and ketone group oxidation process and then the C7 ($m/z = 401.1$) and C8 ($m/z = 323$) resulted. Noteworthily, the were detected opening ring intermediates, including C_9 ($m/z = 222.1$), C_{10} ($m/z = 260.1$), C_{11} ($m/z = 177.1$) and TC_{12} ($m/z = 149.1$). These opening ring

intermediates were finally, oxidized into CO_2 and H_2O confirmed by the TOC remove efficiency result in Fig. S8. It is obviously that the TOC removal efficiency for S3-MIL-53(Fe) is over two times higher than that of MIL-53(Fe) indicating a different mineralization of TC degradation. This result indicates that the sulfur modification strategy can endow the high TC degradation and mineralization efficiency.

4. Conclusions

A regular spindle-shaped S-MIL-53(Fe) was successfully synthesized via in-situ encapsulation treatment. The as-synthesized S3-MIL-53(Fe) crystal exhibited superior higher apparent quantum efficiency (AQE) of 27.82% which was over 30 times than that of pure MIL-53(Fe) (0.903%) indicating the significantly enhanced tetracycline photocatalytic degradation efficiency under visible light irradiation. The enhanced photocatalytic performance can be attributed to architectural preponderance and more efficient photo-excitation. Specifically, an intermediate energy level for S-MIL-53(Fe) was formed resulting in a much easier photoexcited way for electrons jumping up to the middle energy level from the valence band. Meanwhile, the developed S3-MIL-53(Fe) showed an excellent and extensive ability to degrade TC in the river and trap water environment with good stability and reusability. The specific TC degradation process on S3-MIL-53(Fe) was also investigated by the LC-MS technique and the possible degradation pathways were also proposed. All in all, this work provides a valuable reference in intramolecular modulation iron-based metal organic framework family to prepare efficient photocatalyst. And this proposed practice will undoubtedly make contributions to the photocatalytic purification technology of organic pollutant wastewater.

CRediT authorship contribution statement

Haoyun Chen: Investigation, Writing – original draft preparation, Calculation, Writing, Revision, Writing – review & editing. **Xingzhong Yuan**: Validation, Resources, Writing – review & editing. **Longbo Jiang**: Conceptualization, Writing, Revision, Resources, Writing – review & editing. **Hou Wang**: Calculation, Writing, Revision, Writing – review & editing. **Hanbo Yu**: Visualization, Writing – review & editing. **Xinxin Wang**: Investigation, Writing – review & editing.
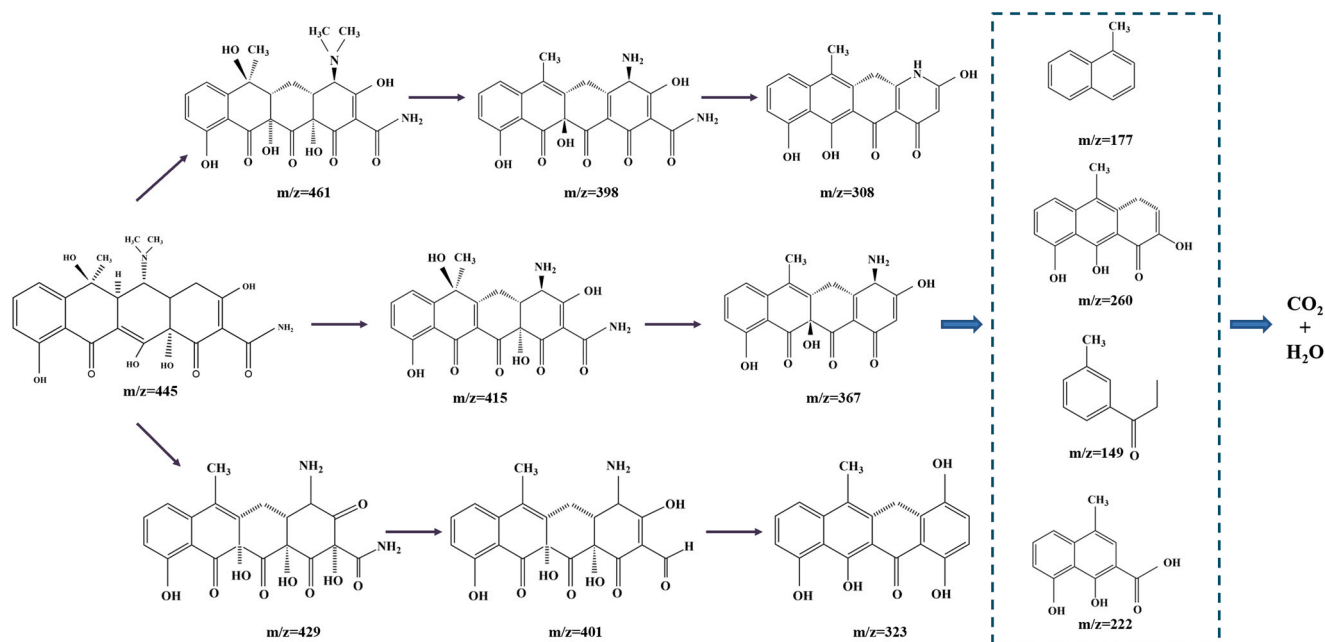

48

Fig. 8. Proposed degradation pathway for tetracycline transformation in S3-MIL-53(Fe) photocatalytic system.

Declaration of Competing Interest

Acknowledgments

Appendix A. Supporting information

Supplementary data associated with this article can be found in the online version at doi:10.1016/j.apcatb.2021.120823.

References

[1] Y. Zheng, Y. Liu, X. Guo, Z. Chen, W. Zhang, Y. Wang, X. Tang, Y. Zhang, Y. Zhao, Sulfur-doped g-C₃N₄/rGO porous nanosheets for highly efficient photocatalytic degradation of refractory contaminants, J. Mater. Sci. Technol. 41 (2020) 117–126, https://doi.org/10.1016/j.jmst.2019.09.018.

[2] W. Fei, Y. Song, N. Li, D. Chen, Q. Xu, H. Li, J. He, J. Lu, Hollow In₂O₃@ZnFe₂O₄ heterojunctions for highly efficient photocatalytic degradation of tetracycline under visible light, Environ. Sci. Nano 6 (2019) 3123–3132, https://doi.org/10.1039/C9EN00811J.

[3] J. Cao, S. Sun, X. Li, Z. Yang, W. Xiong, Y. Wu, M. Jia, Y. Zhou, C. Zhou, Y. Zhang, Efficient charge transfer in aluminum-cobalt layered double hydroxide derived from Co-ZIF for enhanced catalytic degradation of tetracycline through peroxymonosulfate activation, Chem. Eng. J. 382 (2020), 122802, https://doi.org/10.1016/j.cej.2019.122802.

[4] C. Hu, X. Hu, R. Li, Y. Xing, MOF derived ZnO/C nanocomposite with enhanced adsorption capacity and photocatalytic performance under sunlight, J. Hazard. Mater. 385 (2020), 121599, https://doi.org/10.1016/j.jhazmat.2019.121599.

[5] H. Hong, J. Liu, H. Huang, C. Atangana Etogo, X. Yang, B. Guan, L. Zhang, Ordered macro-microporous metal-organic framework single crystals and their derivatives for rechargeable aluminum-ion batteries, J. Am. Chem. Soc. 141 (2019) 14764–14771, https://doi.org/10.1021/jacs.9b06957.

[6] M.J. Valero-Romero, J.G. Santaclara, L. Oar-Arteta, L. van Koppen, D.Y. Osadchii, J. Gascon, F. Kapteijn, Photocatalytic properties of TiO₂ and Fe-doped TiO₂ prepared by metal organic framework-mediated synthesis, Chem. Eng. J. 360 (2019) 75–88, https://doi.org/10.1016/j.cej.2018.11.132.

[7] Y. Pi, S. Jin, X. Li, S. Tu, Z. Li, J. Xiao, Encapsulated MWCNT@MOF-derived In₂S₃ tubular heterostructures for boosted visible-light-driven degradation of tetracycline, Appl. Catal. B Environ. 256 (2019), 117882, https://doi.org/10.1016/j.apcatb.2019.117882.

[8] B.N. Bhadra, A. Vinu, C. Serre, S.H. Jhung, MOF-derived carbonaceous materials enriched with nitrogen: preparation and applications in adsorption and catalysis, Mater. Today 25 (2019) 88–111, https://doi.org/10.1016/j.mattod.2018.10.016.

[9] Q. Xia, H. Wang, B. Huang, X. Yuan, J. Zhang, J. Zhang, L. Jiang, T. Xiong, G. Zeng, State-of-the-art advances and challenges of iron-based metal organic frameworks from attractive features, synthesis to multifunctional applications, Small 15 (2019), 1803088, https://doi.org/10.1002/smll.201803088.

[10] N.C. Sanchez, J.L. Guzman-Mar, L. Hinojosa-Reyes, G.T. Palomino, C.P. Cabello, Carbon composite membrane derived from MIL-125-NH2 MOF for the enhanced extraction of emerging pollutants, Chemosphere 231 (2019) 510–517, https://doi.org/10.1016/j.chemosphere.2019.05.173.

[11] M.A. Ahsan, E. Deemer, O. Fernandez-Delgado, H. Wang, M.L. Curry, A.A. El-Gendy, J.C. Noveron, Fe nanoparticles encapsulated in MOF-derived carbon for the reduction of 4-nitrophenol and methyl orange in water, Catal. Commun. 130 (2019), 105753, https://doi.org/10.1016/j.catcom.2019.105753.

[12] R. Liu, L. Ran, B. Niu, Y. Wei, Carbonization of Fe-based metal organic frameworks with mesoporous structure as electrocatalyst for catalysis of oxygen to hydrogen peroxide, J. Nanosci. Nanotechnol. 18 (2018) 4667–4674, https://doi.org/10.1166/jnn.2018.15311.

[13] W. Lu, Z. Wei, Z.Y. Gu, T.F. Liu, J. Park, M. Zhang, Q. Zhang, T. Gentle, M. Bosch, Zhou H.C. Tian, Tuning the structure and function of metal-organic frameworks via linker design, Chem. Soc. Rev. 43.16 (2014) 5561–5593, https://doi.org/10.1039/c4cs00003j.

[14] P. George, Pr. Chowdhury, Enhanced photocatalytic performance of novel S2−doped MIL-53(Fe) under visible light, J. Alloys Compd. 850 (2021) 15657, https://doi.org/10.1016/j.jallcom.2020.156578.

[15] S.-W. Lv, J.-M. Liu, N. Zhao, C.-Y. Li, Z.-H. Wang, S. Wang, A novel cobalt doped MOF-based photocatalyst with great applicability as an efficient mediator of peroxydisulfate activation for enhanced degradation of organic pollutants, New J. Chem. 44 (2020) 1245–1252, https://doi.org/10.1039/C9NJ05503G.

[16] M. Xie, Y. Ma, D. Lin, C. Xu, F. Xie, W. Zeng, Bimetal-organic framework MIL-53 (Co-Fe): an efficient and robust electrocatalyst for the oxygen evolution reaction, Nanoscale 12 (2020) 67–71, https://doi.org/10.1039/C9NR06883J.

[17] S. Chen, Y. Yan, P. Hao, M. Li, J. Liang, J. Guo, Y. Zhang, S. Chen, W. Ding, X. Guo, Iron nanoparticles encapsulated in S,N-codoped carbon: sulfur doping enriches surface electron density and enhances electrocatalytic activity toward oxygen reduction, ACS Appl. Mater. Interfaces 12 (2020) 686–695, https://doi.org/10.1021/acsami.9b20007.

[18] H. Lv, Y. Huang, R.T. Koodali, G. Liu, Y. Zeng, Q. Meng, M. Yuan, Synthesis of sulfur-doped 2D graphitic carbon nitride nanosheets for efficient photocatalytic degradation of phenol and hydrogen evolution, ACS Appl. Mater. Interfaces 12 (2020) 12656–12667, https://doi.org/10.1021/acsami.9b19057.

[19] H. Jin, H. Zhou, D. He, Z. Wang, Q. Wu, Q. Liang, S. Liu, S. Mu, MOF-derived 3D Fe-N-S co-doped carbon matrix/nanotube nanocomposites with advanced oxygen reduction activity and stability in both acidic and alkaline media, Appl. Catal. B Environ. 250 (2019) 143–149, https://doi.org/10.1016/j.apcatb.2019.03.013.

[20] G. Zhao, A. Wang, W. He, Y. Xing, X. Xu, 2D new nonmetal photocatalyst of sulfur-doped h-bn nanosheets with high photocatalytic activity, Adv. Mater. Interfaces 6 (2019), 1900062, https://doi.org/10.1002/admi.201900062.

[21] N. Liu, W. Huang, M. Tang, C. Yin, B. Gao, Z. Li, L. Tang, J. Lei, L. Cui, X. Zhang, In-situ fabrication of needle-shaped MIL-53(Fe) with 1T-MoS2 and study on its enhanced photocatalytic mechanism of ibuprofen, Chem. Eng. J. 359 (2019) 254–264, https://doi.org/10.1016/j.cej.2018.11.143.

[22] Q. Xia, H. Huang, X. Yuan, H. Wang, Z. Wu, L. Jiang, T. Xiong, J. Zhang, G. Zeng, H. Wang, Modified stannous sulfide nanoparticles with metal-organic framework: toward efficient and enhanced photocatalytic reduction of chromium (VI) under visible light, J. Colloid Interface Sci. 530 (2018) 481–492, https://doi.org/10.1016/j.jcis.2018.05.015.

[23] G. Chaturvedi, A. Kaur, S.K. Kansal, CdS-decorated MIL-53(Fe) microrods with enhanced visible light photocatalytic performance for the degradation of ketorolac tromethamine and mechanism insight, J. Phys. Chem. C 123 (27) (2019) 16857–16867, https://doi.org/10.1021/acs.jpcc.9b04312.

[24] W. Mei, D. Li, H. Xu, J. Zan, L. Sun, Q. Li, B. Zhang, Y. Wang, D. Xia, Effect of electronic migration of MIL-53(Fe) on the activation of peroxymonosulfate under visible light, Chem. Phys. Lett. 706 (2018) 694–701, https://doi.org/10.1016/j.cplett.2018.07.020.

[25] Q. Zhang, J.B. Liu, L. Chen, C.X. Xiao, P. Chen, S. Shen, J.K. Guo, C.T. Au, S.F. Yin, An etching and re-growth method for the synthesis of bismuth ferrite/MIL-53(Fe) nanocomposite as efficient photocatalyst for selective oxidation of aromatic alcohols, Appl. Catal. B Environ. 264 (November 2019) (2020), 118529, https://doi.org/10.1016/j.apcatb.2019.118529.

[26] Y. Guo, Z. Zeng, Y. Zhu, Z. Huang, Y. Cui, J. Yang, Catalytic oxidation of aqueous organic contaminants by persulfate activated with sulfur-doped hierarchically porous carbon derived from thiophene, Appl. Catal. B Environ. 220 (August 2017) (2018) 635–644, https://doi.org/10.1016/j.apcatb.2017.08.073.

[27] H. Wang, Y. Bian, J. Hu, L. Dai, Highly crystalline sulfur-doped carbon nitride as photocatalyst for efficient visible-light hydrogen generation, Appl. Catal. B Environ. 238 (July) (2018) 592–598, https://doi.org/10.1016/j.apcatb.2018.07.023.

[28] L. Jiang, X. Yuan, G. Zeng, Z. Wu, J. Liang, X. Chen, L. Leng, H. Wang, H. Wang, Metal-free efficient photocatalyst for stable visible-light photocatalytic degradation of refractory pollutant, Appl. Catal. B Environ. 221 (2018) 715–725, https://doi.org/10.1016/j.apcatb.2017.09.059.

[29] M. Jourshabani, Z. Shariatinia, A. Badiei, Sulfur-doped mesoporous carbon nitride decorated with Cu particles for efficient photocatalytic degradation under visible-light irradiation, J. Phys. Chem. C 121 (2017) 19239–19253, https://doi.org/10.1021/acs.jpcc.7b05556.

[30] H. Huang, K. Xiao, F. Dong, J. Wang, X. Du, Y. Zhang, Sulfur-doping synchronously ameliorating band energy structure and charge separation achieving decent visible-light photocatalysis of Bi₂O₂CO₃, RSC Adv. 6 (2016) 361–364, https://doi.org/10.1039/C6RA04888A.

[31] Q. Liang, M. Zhang, C. Liu, S. Xu, Z. Li, Sulfur-doped graphitic carbon nitride decorated with zinc phthalocyanines towards highly stable and efficient photocatalysis, Appl. Catal. A Gen. 519 (2016) 107–115, https://doi.org/10.1016/j.apcata.2016.03.033.

[32] F. Yi, H. Gan, H. Jin, W. Zhao, K. Zhang, H. Jin, H. Zhang, Y. Qian, J. Ma, Sulfur-and chlorine-co-doped g-C₃N₄ nanosheets with enhanced active species generation for boosting visible-light photodegradation activity, Sep. Purif. Technol. 233 (2020), 115997, https://doi.org/10.1016/j.seppur.2019.115997.

[33] C. Regmi, Y.K. Kshetri, R.P. Pandey, S.W. Lee, Visible-light-driven S and W co-doped dendritic BiVO₄ for efficient photocatalytic degradation of naproxen and its mechanistic analysis, Mol. Catal. 453 (2018) 149–160, https://doi.org/10.1016/j.mcat.2018.05.008.

[34] X. Wei, H. Feng, L. Li, J. Gong, K. Jiang, S. Xue, P.K. Chu, Synthesis of tetragonal prismatic γ-In₂Se₃ nanostructures with predominantly {110} facets and photocatalytic degradation of tetracycline, Appl. Catal. B Environ. 260 (2020), 118218, https://doi.org/10.1016/j.apcatb.2019.118218.

[35] T. Xu, R. Zou, X. Lei, X. Qi, Q. Wu, W. Yao, Q. Xu, New and stable g-C₃N₄/HAp composites as highly efficient photocatalysts for tetracycline fast degradation, Appl. Catal. B Environ. 245 (2019) 662–671, https://doi.org/10.1016/j.apcatb.2019.01.020.

[36] X. Chen, H. Sun, J. Zhang, Y. Guo, D.-H. Kuo, Cationic S-doped TiO₂/SiO₂ visible-light photocatalyst synthesized by co-hydrolysis method and its application for organic degradation, J. Mol. Liq. 273 (2019) 50–57, https://doi.org/10.1016/j.molliq.2018.10.021.

[37] R.F. Yuan, Y.D. Zhu, B.H. Zhou, J.Y. Hu, Photocatalytic oxidation of sulfamethoxazole in the presence of TiO$_2$: effect of matrix in aqueous solution on decomposition mechanisms, Chem. Eng. J. 359 (2019) 1527–1536, https://doi.org/10.1016/j.cej.2018.11.019.

[38] M.O. Alfred, M.O. Omorogie, O. Bodede, R. Moodley, A. Ogunlaja, O.G. Adeyemi, C. Günter, A. Taubert, I. Iermak, H. Eckert, I.D.A. Silva, A.S.S. de Camargo, A. de Jesus Motheo, S.M. Clarke, E.I. Unuabonah, Solar-active clay-TiO$_2$ nanocomposites prepared via biomass assisted synthesis: efficient removal of ampicillin, sulfamethoxazole and artemether from water, Chem. Eng. J. 398 (2020), 125544, https://doi.org/10.1016/j.cej.2020.125544.

[39] Y.R. Lin, G.V.C. Dizon, K. Yamada, C.Y. Liu, A. Venault, H.Y. Lin, M. Yoshida, C. Hu, Sulfur-doped g-C$_3$N$_4$ nanosheets for photocatalysis: Z-scheme water splitting and decreased biofouling, J. Colloid Interface Sci. 567 (2020) 202–212, https://doi.org/10.1016/j.jcis.2020.02.017.

[40] C. Tian, H. Zhao, H. Sun, K. Xiao, P. Keung Wong, Enhanced adsorption and photocatalytic activities of ultrathin graphitic carbon nitride nanosheets: kinetics and mechanism, Chem. Eng. J. 381 (2020), 122760, https://doi.org/10.1016/j.cej.2019.122760.

[41] K. Wu, D. Chen, J. Fang, S. Wu, F. Yang, X. Zhu, Z. Fang, One-step synthesis of sulfur and tungstate co-doped porous g-C$_3$N$_4$ microrods with remarkably enhanced visible-light photocatalytic performances, Appl. Surf. Sci. 462 (2018) 991–1001, https://doi.org/10.1016/j.apsusc.2018.07.221.

[42] H. Yu, B. Huang, H. Wang, X. Yuan, L. Jiang, Z. Wu, J. Zhang, G. Zeng, Facile construction of novel direct solid-state Z-scheme AgI/BiOBr photocatalysts for highly effective removal of ciprofloxacin under visible light exposure: mineralization efficiency and mechanisms, J. Colloid Interface Sci. 522 (2018) 82–94, https://doi.org/10.1016/j.jcis.2018.03.056.

[43] M. Jourshabani, Z. Shariatinia, G. Achari, C.H. Langford, A. Badiei, Facile synthesis of NiS$_2$ nanoparticles ingrained in a sulfur-doped carbon nitride framework with enhanced visible light photocatalytic activity: two functional roles of thiourea, J. Mater. Chem. A 6 (2018) 13448–13466, https://doi.org/10.1039/C8TA03068E.

[44] X. Yuan, L. Jiang, J. Liang, Y. Pan, J. Zhang, H. Wang, L. Leng, Z. Wu, R. Guan, G. Zeng, In-situ synthesis of 3D microsphere-like In$_2$S$_3$/InVO$_4$ heterojunction with efficient photocatalytic activity for tetracycline degradation under visible light irradiation, Chem. Eng. J. 356 (2019) 371–381, https://doi.org/10.1016/j.cej.2018.09.079.

[45] Y. Gao, J. Xia, D. Liu, R. Kang, G. Yu, S. Deng, Synthesis of mixed-linker Zr-MOFs for emerging contaminant adsorption and photodegradation under visible light, Chem. Eng. J. 378 (2019) 122118, https://doi.org/10.1016/j.cej.2019.122118.

[46] L. Jian, Y. Yu, Q. Ruilian, C. Changyan, Z. Yujun, S. Weiguo, Enhanced electron separation on in-plane benzene-ring doped g-C$_3$N$_4$ nanosheets for visible light photocatalytic hydrogen evolution, Appl. Catal. B Environ. 244 (2019) 459–464, https://doi.org/10.1016/j.apcatb.2018.11.070.

[47] Z. Dandan, Z. Qixing, Nitrogen doped g-C$_3$N$_4$ with the extremely narrow band gap for excellent photocatalytic activities under visible light, Appl. Catal. B Environ. 281 (2021), 119474, https://doi.org/10.1016/j.apcatb.2020.119474.

[48] C. Wen, C. Lvcun, L. Jieyuan, Z. Ying, S. Yanjuan, J. Guangming, S.C. Lee, D. Fan, Ba-vacancy induces semiconductor-like photocatalysis on insulator BaSO$_4$, Appl. Catal. B Environ 253 (2019) 293–299, https://doi.org/10.1016/j.apcatb.2019.04.070.

[49] X. Haomin, X. Shibo, L. Jing, L. Shikai, L. Pin, Y. Wei, S. Tao, Q. Dongchen, H. Qian, X. Hai, L. Ming, W. Jishan, Z. Jia, L. Jiong, Chemical design and synthesis of superior single atom electrocatalysts via in situ polymerization, J. Mater. Chem. A 8 (2020) 17683–17690, https://doi.org/10.1039/D0TA05130F.

[50] X. Juanding, J. Hailong, Metal-organic frameworks for photocatalysis and photothermal catalysis, Acc. Chem. Res. 52 (2019) 356–366, https://doi.org/10.1021/acs.accounts.8b00521.

[51] Z. Qingchun, L. Jianga, J. Wanga, Z. Yongfa, P. Yujuan, D. Weidong, Photocatalytic degradation of tetracycline antibiotics using three-dimensional network structure perylene diimide supramolecular organic photocatalyst under visible-light irradiation, Appl. Catal. B Environ. 277 (2020) 119–122, https://doi.org/10.1016/j.apcatb.2020.119122.